

In-Depth Compositional Analysis of the Carbon-Rich Fine-Grain Layer in Solution-Processed CZTSSe Films Accessed by a Photonic Lift-Off Process

Ahmed Javed, Michael Jones, Stephen Campbell, Selcuk Yerci,* Vincent Barrioz, and Yongtao Qu*

The existence of a fine-grain (FG) sub-layer between the top large-grain (LG) layer and the back contact is widely observed in kesterite absorbers prepared with organic solvents. In this paper, the distinguishing features of the lifted-off carbon-rich FG layer are investigated through direct analysis with a series of characterization techniques, including X-ray photoelectron spectroscopy (XPS), attenuated total reflectance, X-ray diffraction, and scanning electron microscopy. To access the FG layer for direct probing, a scalable and repeatable photonic lift-off method is developed for carrying out the separation of the kesterite absorber layer from the Mo-coated glass substrate. A very high light intensity of 4 kW cm^{-2} for a short interval of 1 ms is optimized by COMSOL simulations, and successful implementation is demonstrated. The XPS analysis has revealed significant carbon content at the exposed FG surface, which explains the hindrance of grain growth due to carbon abundance. The variations in cations and anions concentrations from FG layer leading into LG region are explored through argon ions (Ar^+) assisted XPS depth profiling. The observed significant differences between the composition of FG and LG regions are speculated to negatively impact the performance of solar cells.

direct bandgap (1–1.5 eV).^[2,3] However, the scarcity and high prices of In and Ga make kesterite a favorable candidate for thin film solar cell applications.^[4–6] CZTSSe absorbers developed from vacuum-based techniques, such as co-evaporation and co-sputtering, have shown respectable thin film solar cell efficiencies (>10%).^[7,8] Additionally, non-vacuum techniques, also known as solution processing methods, have recently become a preferable synthesis choice owing to their cost effectiveness, better phase control, and high throughput.^[9] Moreover, they have the power to be compatible with high-volume and high-value manufacturing with a variety of possible substrates, including flexible foils, plastics, and ultra-thin glass.^[10,11] Molecular and nanoparticle ink synthesis has become a dominant solution-based strategy to fabricate kesterite absorbers.^[12,13] In a typical ink synthesis, the metal precursors featuring cations are dissolved together (with or without sulfur source)

in a high boiling point solvent to make a dispersive and stable solution for nanoparticles formed through the burst nucleation process.^[14] The prepared ink is then coated on a rigid substrate (mostly soda lime glass) by means of spin coating,^[15] doctor blading,^[16] or spray coating.^[17] Subsequently, the deposited film is annealed in a selenium or sulfur environment to

1. Introduction


Kesterite $\text{Cu}_2\text{ZnSnS}_x\text{Se}_{4-x}$ (CZTSSe) solar cell is a promising alternative to other thin film PV devices due to its Earth-abundant, distinct optical and electronic properties.^[1] Closely related to the prominent chalcopyrite (CIGSSe) thin-film technology, CZTSSe also has a high absorption coefficient ($\approx 10^4 \text{ cm}^{-1}$) and a tunable

A. Javed, S. Yerci
 Department of Micro and Nanotechnology
 Middle East Technical University
 Ankara 06800, Turkiye
 E-mail: syerci@metu.edu.tr

A. Javed, S. Yerci
 Center for Solar Energy Research and Applications (GUNAM)
 Middle East Technical University
 Ankara 06800, Turkiye

M. Jones, S. Campbell, V. Barrioz, Y. Qu
 Department of Mathematics, Physics, Electrical Engineering
 Northumbria University
 Newcastle Upon Tyne NE1 8ST, UK
 E-mail: y.qu@northumbria.ac.uk

S. Yerci
 Department of Electrical and Electronics Engineering
 Middle East Technical University
 Ankara 06800, Turkiye

 The ORCID identification number(s) for the author(s) of this article can be found under <https://doi.org/10.1002/admi.202300715>

© 2023 The Authors. Advanced Materials Interfaces published by Wiley-VCH GmbH. This is an open access article under the terms of the Creative Commons Attribution License, which permits use, distribution and reproduction in any medium, provided the original work is properly cited.

DOI: 10.1002/admi.202300715

execute grain growth and get the desired chemical composition of the kesterite nanocrystals.^[15] In recent years, the efficiencies of kesterite solar cells developed with low-cost and facile solution processing techniques have been seen as comparable to expensive vacuum methods.^[18] In fact, hydrazine, being used as a solvent for kesterite absorber layer synthesis, has been known to provide CZTS(Se) solar cells with high power conversion efficiencies ($\approx 13\%$) at the laboratory scale.^[19,20] On the other hand, alternative non-toxic organic solvents have gained more attention in recent years for both CZTS and CIGS nanoparticle ink preparation processes.^[21] Oleylamine (OLA) is ubiquitously used as an organic solvent for CZTS ink preparation due to its ability to create a homogenous, stable, and dispersive ink which is instrumental in achieving high PV performances.^[13,22] However, CZTS(Se) films prepared with organic solvents have shown the presence of a carbon-rich FG sub-layer between the LG layer and the back contact (usually molybdenum) after high-temperature annealing.^[23,24] As the CZTS nanoparticles are formed, the OLA-based ligands comprised of long hydrocarbon chains surround the nanocrystal surface by forming a strong bond between nitrogen atom from the OLA molecule and cations in kesterite crystal.^[25] After annealing, the ligand's bulky chains decompose and the carbon residues mostly reside at the rear end of the absorber layer restricting the grain growth, thereby giving rise to a bi-layer structure comprising of LG and FG.^[26,27] Some efforts have been made to understand the implication of this FG layer on the performance of solar cells.^[28–30] It is likely to reduce device performance via carrier recombination through traps, defect states,^[31] charge transport issues,^[32] enhanced series resistance,^[33] and an increased grain boundary density.^[34] However, Wu et al.^[35] claimed that the carbon-rich FG layer has no adverse effect on the device's performance after conducting a modeling analysis of the bi-layer structure by experimentally calculating its optical properties. Moreover, Park et al.^[36] concluded that the carbon-rich layer is in the form of an amorphous state and acts as a favorable conductive path for the passage of charge carriers. A direct probing method would allow an accurate and improved understanding of the FG layer. A thorough investigation in terms of an accurate compositional study of the FG layer (in junction with glass substrate) seems an arduous task due to the difficulty of its direct access. Even though some efforts have previously been made using mechanical lift-off and laser scribing methods to expose the rear side,^[37,38] a direct, in-depth, and systematic study of the FG layer on solution-processed kesterite absorbers has not been thoroughly explored in the literature. Moreover, in a mechanical lift-off process, the exertion of immense force to peel-off a semiconductor layer from the substrate can induce significant cracks on the lifted-off film which might hinder charge transport.^[39–42] On the other hand, a laser lift-off is a known technique commonly used in industry for separating films from growth substrates; however, the operation requires careful maintenance of power value and full-width half maximum (FWHM) of the laser beam that results in slow throughput.^[43,44] Furthermore, an excimer laser operating at an ultra-violet wavelength can cause ashing of polymer and/or organic films during the scribing process.^[45] Wet chemical lift-off techniques have also been used to separate thin films from growth substrates; however, the employment of a sacrificial layer (to be etched away in an etchant solvent) requires additional pro-

cessing steps and the strong nature of etchant solvent, i.e., hydrofluoric acid, can harmfully react with other layers as well.^[46–49] A PLO method involves high-intensity light absorbance in a single layer triggering a clean separation from the substrate while a faster light scan can yield a higher throughput as compared to a high-cost laser lift-off technique.^[50,51] One of the important findings of this research is to invoke a reliable method to lift-off absorber layer along with all the front layers, namely cadmium sulfide (CdS), zinc oxide (ZnO), and indium tin oxide (ITO), thus not only exposing FG side for direct compositional analysis but also devising a method to transfer the solar cell structure from rigid glass substrate to a flexible substrate, thereby leading a promising pathway for system integrated photovoltaic applications (SIPV) as part of future research. In this research, a rapid, scalable, and reliable photothermal technique was developed by using a very short pulse of broadband light to PLO solar cells from growth substrates. It found the top solar cell structure separating from the bottom growth substrate at the $\text{MoSe}_2/\text{CZTSSe}$ interface and the feasibility of this technique has been verified by our XRD measurement as well as Raman spectroscopy and energy-dispersive X-ray spectroscopy (EDS) results (given in supporting information). This established PLO approach demonstrates a repeatable method to expose the rear side (carbon-rich end) of the light absorber layer, opening up the possibility of understanding the FG layer directly and extensively using different characterization techniques. The insights developed from a direct depth profiling done on the exposed rear side of the CZTSSe layer can reveal important features of the carbon-rich FG layer. Some efforts have previously been made using chemical etching techniques to remove a portion of the layer for extracting compositional information beneath the sample surface.^[52–55] Tiwari et al., have used a bromine solution to partially etch a kesterite layer for depth profiling.^[55] Although this technique is feasible, it requires tedious chemical procedures. The treated samples should be examined quickly after chemical treatment and must be kept in a vacuum environment to avoid degradation. Furthermore, controlling the etch rate remains to be a challenge in wet chemical methods.

In this work, we have adopted a standard Ar^+ sputtering technique for XPS depth profiling to understand the concentration trends of carbon and absorber's component elements from FG to LG layer in an OLA-based solution-processed CZTSSe bilayer structure. The built-in Ar^+ sputtering tool in an XPS instrument serves to be a faster and convenient method for depth profiling which also gives better control over the etch rate simply by adjusting sputter parameters. Our in-depth XPS analysis revealed that on average carbon covers almost 50% of the elemental content in the perceived FG layer while the cation contribution is even less than 3%. The carbon-rich content has been confirmed by the ATR measurements, which showed distinctive C–H peaks between 2848 and 2955 cm^{-1} .

In the following sections, a discussion of the lift-off process using a pulse forge system is provided and the characterization measurements on the lifted-off samples are systematically performed. According to authors' knowledge, this paper is the first of its kind providing an accurate XPS depth profiling by directly probing the FG layer of kesterite absorber (synthesized by hot injection) exposed by the PLO method.

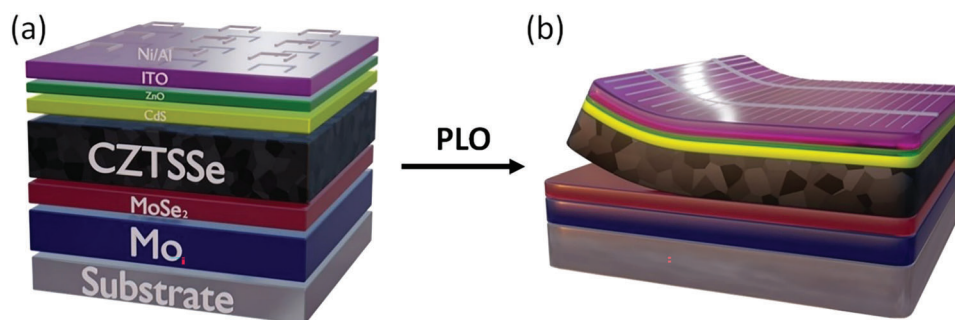


Figure 1. a) Schematic of CZTSSe solar cell configuration. b) Successfully exposing the FG layer at CZTSSe/MoSe₂ interface using PLO.

2. Results and Discussions

2.1. Absorber Photonic Lift-Off

A common structure for a CZTSSe solar cell is the substrate configuration with soda-lime glass as the supporting structure. The subsequent layers are often molybdenum (Mo), CZTSSe, CdS, ZnO, ITO, and metal grids (**Figure 1a**).^[56] To convert nano-sized nanoparticles into efficient light absorbers, an essential high-temperature selenization step is required.^[57] During the high-temperature annealing, a MoSe₂ layer forms between the CZTSSe absorber and Mo substrate, as shown in **Figure 1a**. Whilst the MoSe₂ layer does improve band alignment,^[58,59] the formation of an increasingly thick layer is correlated with a hole barrier, which is observed in both sulfide and selenide systems.^[59] The PV performance (and device fabrication details) of the kesterite structure shown in **Figure 1a** has already been published elsewhere^[13] by some of our co-authors and, in this research, we do not mention any solar cell output since the main motivation of this paper is to analyze FG in depth. To get access to the FG layer at the rear surface, the method of separating the CZTSSe layer at the CZTSSe/MoSe₂ interface is indicated in **Figure 1b**.

The PLO approach utilized a photonic curer (PulseForge Invent IX2-95X). The purpose was to create a short, high-energy pulse of light that would pass through the glass and into the Mo layer. The absorption of pulsed light causes an increase in the temperature. **Figure 2a** shows the temperature profiles at different layers obtained from SimPulse photonic curing simulation software. Relatively high temperatures can be observed in the Mo/MoSe₂ thin films, indicating Mo acts as the heat-absorbing layer. The absorption of the light causes a shock expansion of the Mo/MoSe₂ layers, a resulting effect of the differing thermal expansion coefficients of the neighboring materials. Thus, a complete separation at the CZTSSe/MoSe₂ interface is expected, as shown in **Figure 2b**. The top CZTSSe solar cell structure has been lifted off and transferred to a transparent and flexible substrate (adhesive polyurethane tape manufactured by 3M). COMSOL simulation was further performed in **Figure 2c,d**, showing the heat transfer, and resulting strain (red vector arrows) during the PLO process on a 25 mm × 25 mm substrate. It was found that a pulse energy of around 4 J cm⁻² for a duration of 1 ms (light power density equal to 4 kW cm⁻²) achieved the best CZTSSe absorber lift-off. **Figure 2d** shows a zoomed-in 2D slice of the CZTSSe device on SLG with flexible polyurethane (PU) film on

top. The red and green arrows indicate the resultant strain vectors following a 1 ms light pulse in the x and z directions, respectively. The COMSOL model suggests that the strain in the x direction is highest at the Mo/MoSe₂ interface following the light pulse, leading to the separation of the device stack above this interface.

Upon first inspection, the absorber material has lifted off from the sample entirely, leaving behind no CZTSSe absorber on the growth substrate. SEM and EDS characterization demonstrate strong evidence of a successful lift-off achieved at the interface of the top CZTSSe absorber and bottom MoSe₂/Mo substrate. The SEM images show a columnar Mo structure on the remaining substrate (**Figure 3a**) and grain structures on the absorber underside (**Figure 3b**). In combination, EDS spectroscopy (**Figure S1a**, Supporting Information) shows evidence of residual absorber materials, including Zn and Sn, which remain on the Mo substrate. This is further backed up by the GIXRD performed on the remaining material on the substrate, as shown in **Figure 4**. Peaks from the residual CZTSSe absorber are observed at a shallower incident angle of 0.35° at a depth of ≈15 nm. As the incident angle increases to 0.55° (penetration depth of ≈100 nm), characteristic peaks from the bottom MoSe₂ can be clearly observed. The Raman spectra taken from the top side (before lift-off) and exposed rear side of the lifted-off CZTSSe layer confirm the feasibility of the PLO technique since CZTSe (193.8 cm⁻¹) and CZTS (329.6 cm⁻¹) phases were noticed to be persistent after photonic curing treatment as shown in **Figure S2** (Supporting Information).

In the lifted-off samples, however, no signal from the Mo substrate could be detected in addition to the peaks from CZTSSe, CdS, and ITO layers, as shown in **Figure 4b**. This matches with the EDS data (**Figure S1b**, Supporting Information) that clear signals from all component elements of the CZTSSe absorber, CdS (Cd signal) buffer layer, and ITO (In signal) window layer can be seen. This reveals that there was no detectable Mo on the lifted-off absorber side and verifies a successful separation of the CZTSSe absorber layer from the Mo-coated SLG substrate. This established PLO approach demonstrates a repeatable method to expose the rear surface of the absorber layer, opening up the possibility of accessing the FG layer directly.

2.2. Characterization of the Exposed Lifted-Off Surface

XPS offers a useful analysis in studying the elemental distribution of CZTSSe bi-layer structure (LG and FG) to develop insights into the grain growth mechanism of CZTSSe film prepared with

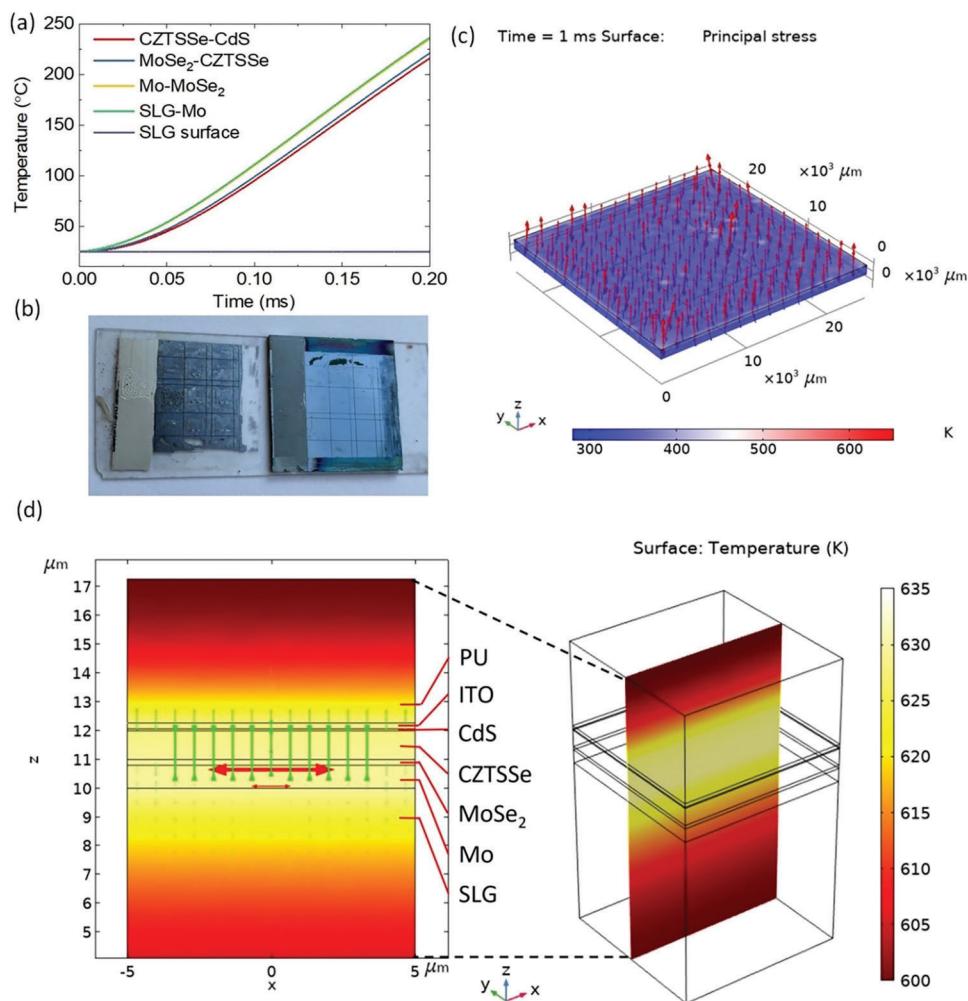


Figure 2. a) The temperature profiles at different interfaces obtained from SimPulse photonic curing simulation software. b) A uniformly lifted-off solar cell (left) and remaining Mo/glass substrate (right). c) COMSOL model showing heat transfer and resulting strain (red vector arrows) during the PLO process on a 25 mm × 25 mm substrate. d) A zoomed-in cross-sectional view to show the strain magnitude in the x and z direction at Mo/MoSe₂ layers.

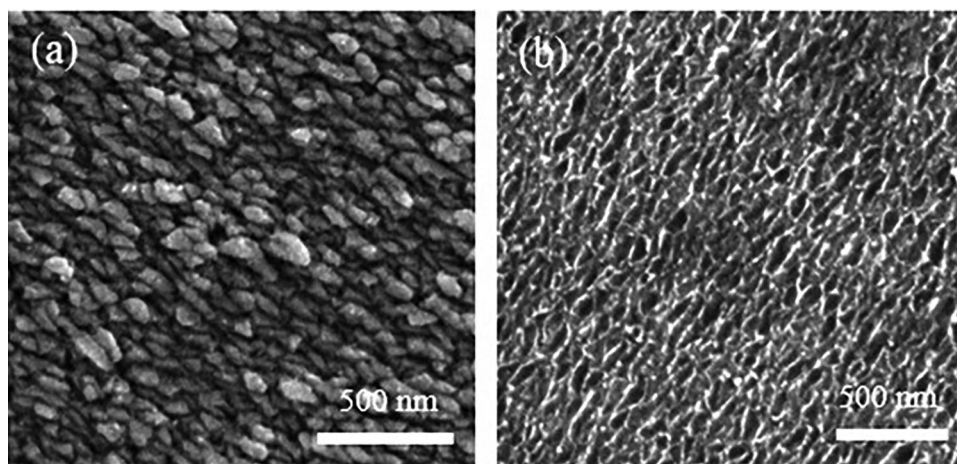


Figure 3. a) SEM image of MoSe₂ columnar structure remaining material on the substrate. b) SEM image of carbon-rich CZTSSe FG surface on the lifted-off absorber layer.

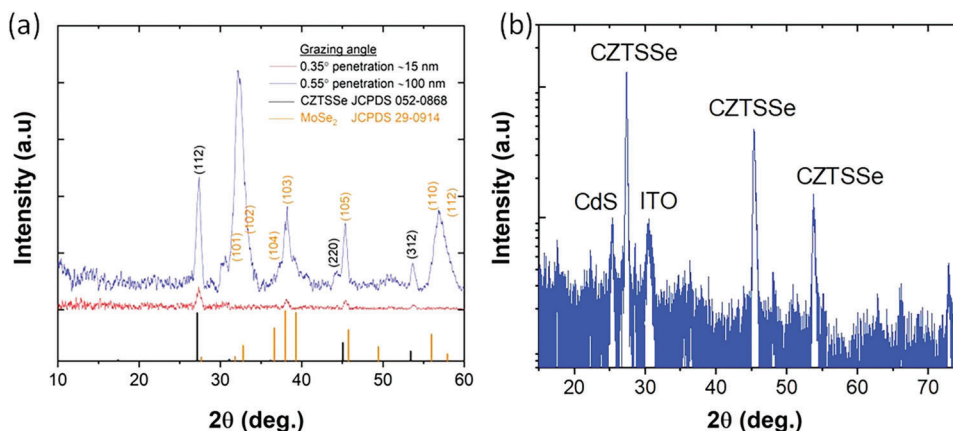


Figure 4. a) Grazing incidence angle X-ray diffractogram of the top surface of the remaining substrate, measured at an incident angle of 0.35° (red) and 0.55° (blue). Black and yellow lines represent peaks belonging to CZTSSe and MoSe_2 , respectively. b) XRD diffractogram of the underside of the lifted-off absorber and top device layers.

a hot injection process, as mentioned in the experimental section. The properties of the exposed FG layer are first investigated, which has allowed an accurate analysis of the elemental composition at the lifted-off surface. A depth profiling assisted by Ar^+ sputtering was then done on the absorber's rear side to analyze the variations and concentration trends of carbon and absorber's component elements at deeper regions of the film leading toward the LG layer. It is interesting to study the profile of the elements in the FG layer to understand the absorber grain growth in the high-temperature annealing process. Ar^+ were sputtered for a total of 65 min, and high-resolution measurements were taken after every 15 min starting from 5 min of sputtering. **Figure 5b** shows the exposed rear surface of the CZTSSe absorber layer used for the XPS study. Compared with the sample surface, the Ar^+ sputtered region depicts fading of color, indicating the removal of the

carbon-rich structure. A typical cross-sectional SEM image of the structure is shown in **Figure 5c**, displaying an exposed FG layer at the rear surface.

High-resolution signals corresponding to the spectra of C and the elements of the absorber layer, namely Cu, Zn, Sn, S, and Se were collected at the surface and multiple depths inside the layer. The XPS peaks corresponding to the elemental concentration of CZTSSe film vary with the increase in sputtering time. The collected spectra of C 1s, Cu 2p, Zn 2p, Sn 3d, S 2p, Se 3p, and Se 3d for surface and at all depths are shown in **Figure 6**. It is quite evident that the carbon peak is sharpest at the surface, and it broadens and shifts to higher binding energies (BE) with the increase of sputtering time. This suggests that the overall peak is convoluted and change in FWHM is caused due to an increased contribution of the broader peak. For a sample that

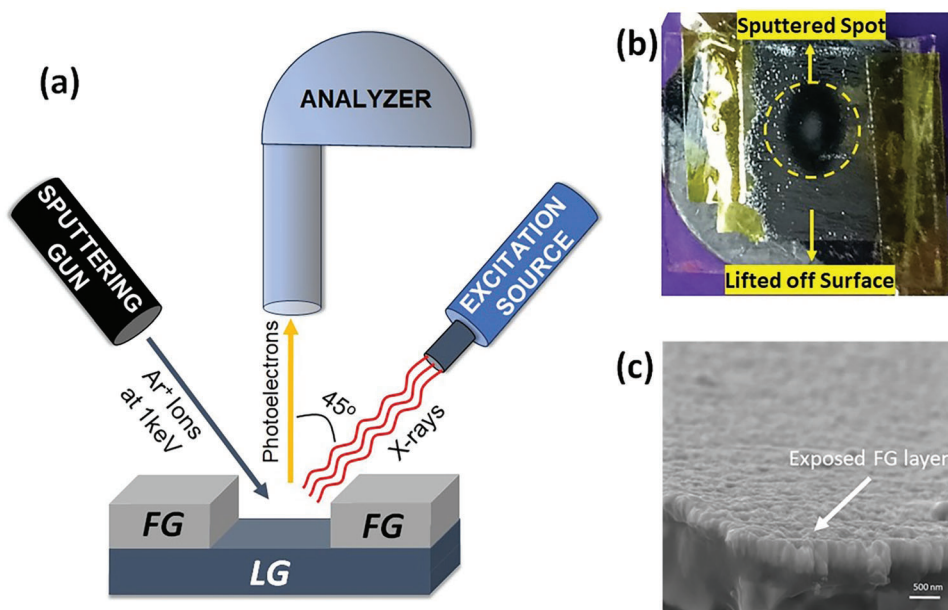


Figure 5. a) Schematic of XPS measurement setup depicting Ar^+ sputtering and FG removal. b) CZTSSe sample with exposed FG layer used for XPS study. c) Cross-sectional SEM image of the surface region showing the exposed FG layer structure.

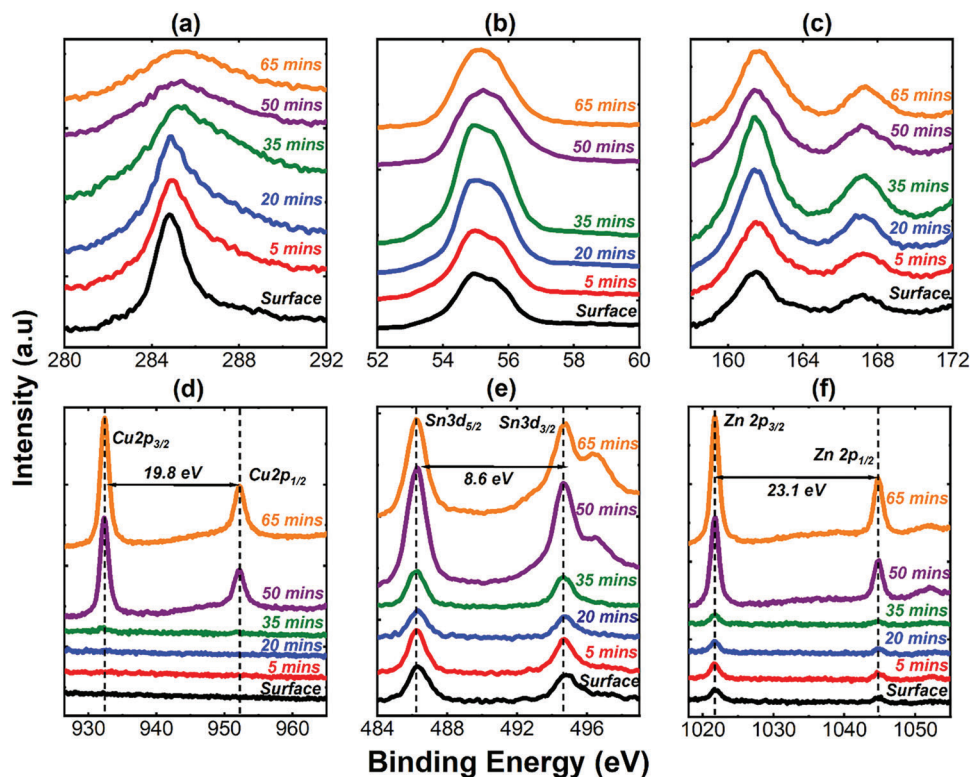


Figure 6. XPS depth profile spectra of; a) C 1s, b) Se 3d, c) S 2p and Se 3p, d) Cu 2p, e) Sn 3d, and f) Zn 2p.

has Se, Se LMM Auger peaks are expected to be found anywhere between 150 and 400 eV,^[60] and overlap XPS spectra of multiple elements.^[61] Therefore, the broader peak can be ascribed to the Se LMM peak as shown in Figure 7. Since carbon is expected to be highest at the surface, the surface peak is assumed to be contributed mostly by C1s, having the lowest FWHM whereas the peak associated with 65 min of sputtering is assumed to be contributed mostly by Se LMM, having the highest FWHM. Furthermore, a shift of 0.7 eV was noticed between the peaks at the

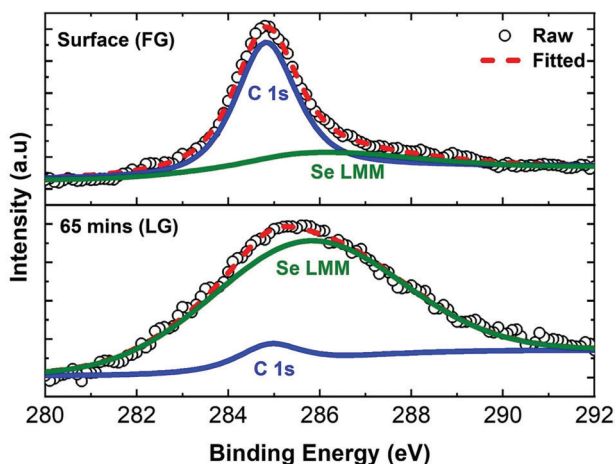


Figure 7. XPS fitting spectra of C for surface and last sputtered depth showing deconvolution of C1s and Se LMM.

surface and the deepest inspected region. While C1s contributed around 85% of the overall peak area at the surface, it dropped down to even less than 5% at 65 min of sputtering depth as depicted in Figure 7. Hence, it can be said that carbon almost diminishes at the final measured depth and the LG layer is reached. LG in the absorber film at such depth is significantly lower in carbon compared to the FG layer at the rear side where carbon has condensed in the high-temperature selenization process and arrested the grain growth. This is expected for solution-processed CZTSSe films as mentioned before. Se3d peaks were found at the surface and all depths thereon as shown in Figure 6b. Se3d_{5/2} and Se3d_{3/2} are convoluted with each other and together form the overall 3d peak centered at 55.1 eV. These Se3d peaks were deconvoluted into two peaks (Se3d_{5/2} and Se3d_{3/2}) with a separation of 0.6 eV. The FWHM of these two sub-peaks was kept equal during the fitting procedure and as expected, Se3d_{5/2} contributed slightly more than 60% of the overall peak area for all measured depths as shown in Figure S3 (Supporting Information).

The presence of Se at the rear surface confirms the diffusion of Se atoms to the rear side of the CZTS film, which indicates a supply of selenium atoms throughout the film. During selenization, an exchange between sulfur and selenium atoms in the lattice is expected owing to their similar properties.^[57] In Figure 6c, it can be easily noticed that there are two peaks centered at 161.5 and 167.1 eV, which are noticeably separated from each other. However, generally, the separation between S2p_{3/2} and S2p_{1/2} peaks is around 1-1.2 eV and these peaks need to be deconvoluted.^[62] This indicates the presence of Se3p peak in the same window, which typically has a spin-orbital splitting of around 6 eV.^[62] Hence, it

can be deduced that the smaller and wider peak at 167.1 eV belongs to $\text{Se}3p_{1/2}$ while the larger peak at 161.5 eV is contributed by $\text{Se}3p_{3/2}$, $\text{S}2p_{1/2}$, and $\text{S}2p_{3/2}$ sub-peaks. Therefore, an accurate elemental analysis requires careful investigation of these two peaks to avoid over/under estimation of S2p and Se3p. The fitting details of all elemental curves at all depths are provided in Figure S2 (Supporting Information).

The peaks of Sn3d and Zn2p were observed at all the measured depths, including the surface as well; however, the peaks became highly intense at the final two measured depths. In the case of Cu2p, the peaks were absent at the surface up to 35 min of sputtering depth and eventually appeared distinctively after 50 min of sputtering. Moreover, a shoulder at the higher BE side of Sn3d_{3/2} spectra, apparent in the last two measured depths, is attributed to Zn-LMM auger signal.^[63] As mentioned in Figure 6d–f, the positions and orbital splitting of Cu, Zn, and Sn peaks confirm +1, +2, and +4 valency of Cu, Zn, and Sn, respectively.^[18,63,64] The effect of concentration trends of absorber elements on the growth process of nanocrystals can be examined from the XPS depth profile data. The absence of Cu and meager concentrations of Zn and Sn from the surface up to 35 min of sputtering depth indicate the importance of cation concentration for the grain growth process. During selenization, the grains enlarge by initially forming copper selenides before Zn and Sn are incorporated into the lattice to complete the CZTSSe nanocrystal structure.^[65] Therefore, Cu-rich conditions are conducive for initial selenization; hence, the absence of Cu–Se phase for depths before 50 min of sputtering can be regarded as a reason for incomplete grain growth. Thereby, we can label the region from the surface up to 35 min of sputtering depth as the FG layer, while the LG layer starts after 50 min of sputtering. Cu–Zn–Sn–S–Se crystals are formed in the LG layer; however, the FG layer is mainly composed of C, S, and Se. Further insights can be developed in the grain growth process by inspecting the infrared (IR) spectra gathered from the top and rear sides of the CZTSSe layer.

ATR measurements taken from the rear side of lifted-off the absorber layer indicate three distinctive peaks at 2955 cm^{-1} , 2917 cm^{-1} , and 2848 cm^{-1} , as shown in Figure 8. Such peaks are peculiar to C–H bonds,^[66] and are not present in the IR spectra gathered from the LG area, thereby suggesting the absence of OLA ligands. These C–H bonds are accompanied by organic ligands covering the nanocrystals to restrict the grain size. Generally, such ligands are expected in nanoparticle films developed with organic solvents and should mostly be evaporated during annealing in which selenium and sulfur atoms assist in the evaporation of carbon atoms by forming a volatile $\text{C}(\text{S},\text{Se})_2$ compound in a high-temperature reaction.^[67,68] However, the existence of a FG layer still occupying the bottom side of CZTSSe film hints toward incomplete evaporation of carbon under the adopted annealing condition for selenization.

The elemental distributions in FG and LG layers are calculated by dividing the fitted peak areas of the measured XPS spectra by their respective relative sensitivity factors (RSF). It is quite clear that C, S, and Se share significantly higher contribution in the FG layer as compared to Sn, Zn, and Cu, therefore these two sets of elements are plotted separately for better representation (C, S, and Se—Figure 9a; Sn, Zn, and Cu—Figure 9b). Figure 9a shows carbon atoms encompassing almost 70% of the

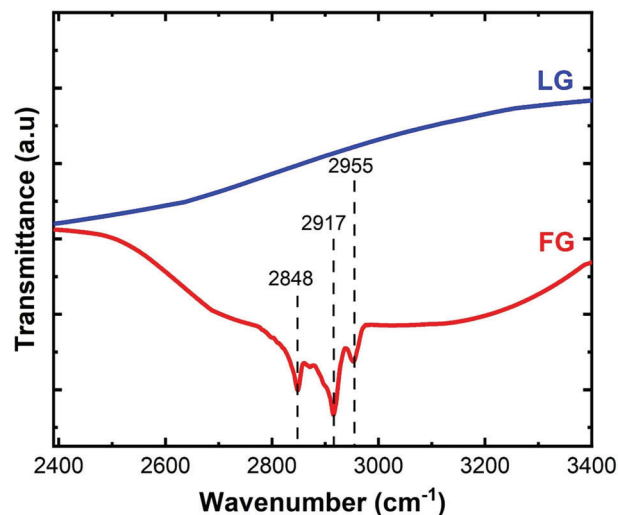


Figure 8. ATR spectra representing the LG and FG regions of the CZTSSe layer where C–H peaks at 2955 cm^{-1} , 2917 cm^{-1} , and 2848 cm^{-1} are marked on the FG curve.

total elemental percentage at the rear surface. It then gradually declines to 7.5% at the last measured depth where the so-called LG layer is reached. The average carbon content, however, remains more than 46.5% in the assumed FG region as depicted in Figure S4 (Supporting Information). Accordingly, the concentrations of Cu, Zn, and Sn increase at deeper regions while S and Se contributions were found to be maximum at 35 min of sputtering depth (the last depth before the LG interface starts). Even though carbon content falls to around 20% at the last measured depth in the FG region (35 min sputtering), the total cations content (Cu+Zn+Sn) is still below 3%, which is not conducive to LG formation of CZTSSe crystals. This also consolidates the concept of out-diffusion of cations from nanoparticles residing at the rear side during annealing.^[65] The average concentrations of each element in the so-called FG and LG are shown in Figure S4 (Supporting Information).

To further investigate FG and LG elemental distributions, some important atomic ratios of multiple elements as a function of sputtering time are shown in Figure 10. Figure 10a suggests that Se concentration remains higher than S for both FG and LG layer with the highest difference noticed at the edge of FG adjacent to LG. Figure 10b confirms Cu poor composition in the LG region, where $\text{Cu}/(\text{Zn}+\text{Sn})$ is found to be 0.71 at the last measured depth. The Zn to Sn ratio trend represented in Figure 10c shows a sharp increase after entering the LG region and becomes 0.93 at the last investigated depth. It is expected that such a trend will lead to Zn-rich composition deeper into the LG layer (which remains undetermined in this work). Figure 10d exhibits a very low (<0.1) ratio of cations (Cu, Zn, and Sn) to anions (Se, and S) in FG but then quickly increases after entering the LG region, suggesting the importance of cations concentration needed for the grain growth process. Lastly, Figure 10e depicts the domination of carbon atoms compared to CZTSSe ones at the rear surface which starts to decline as we go further into FG and becomes extremely small at the last measured depth. This further confirms the dependence of carbon concentration on the grain

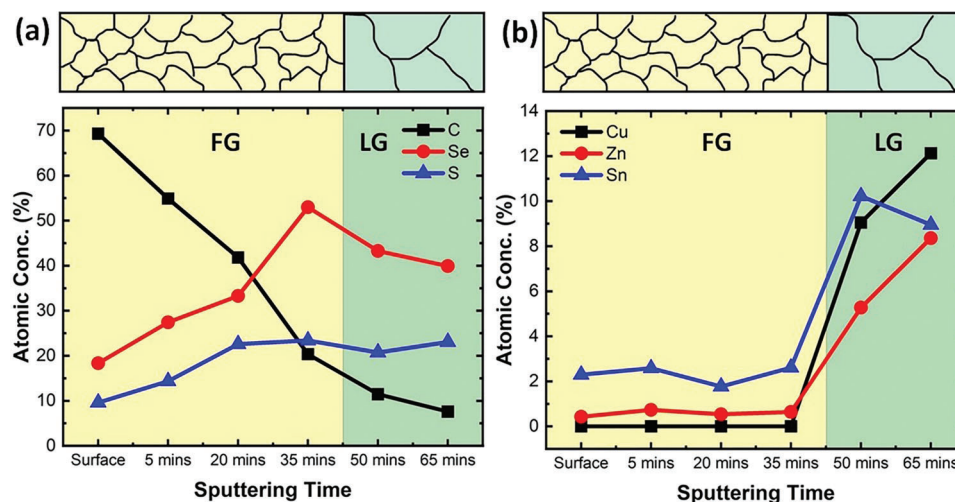


Figure 9. Content percent as a function of sputtering time extracted from fitted curves for a) C, S, and Se and b) Sn, Cu, and Zn.

growth mechanism of CZTSSe crystals. It should be noted that the labeled LG region in Figures 9 and 10 corresponds to the area near the interface between FG and LG regions, therefore, the cation concentrations (Cu, Zn, and Sn) are expected to further rise while anions concentration (Se, and S) is speculated to slightly decrease deep into LG region leading to proper CZTSSe stoichiometry.

Given our in-depth compositional study of this bi-layer absorber structure, it can be conjectured that the PV performance of the solar cell is compromised by the existence of secondary

phases due to such a significant difference between the elemental distribution of FG and LG regions. In addition to this, the total atomic concentration of metals (Cu, Sn, and Zn) being less than 3% in the labeled FG region confirms the insulating nature of the FG layer, which can be regarded as the primary cause of series resistance. Although the use of OLA as a solvent in solution-processed kesterite absorber provides the required dispersibility and stability to the nanoparticles, the performance of the synthesized absorber layer still needs to be improved by addressing the issues raised by our extensive compositional analysis.

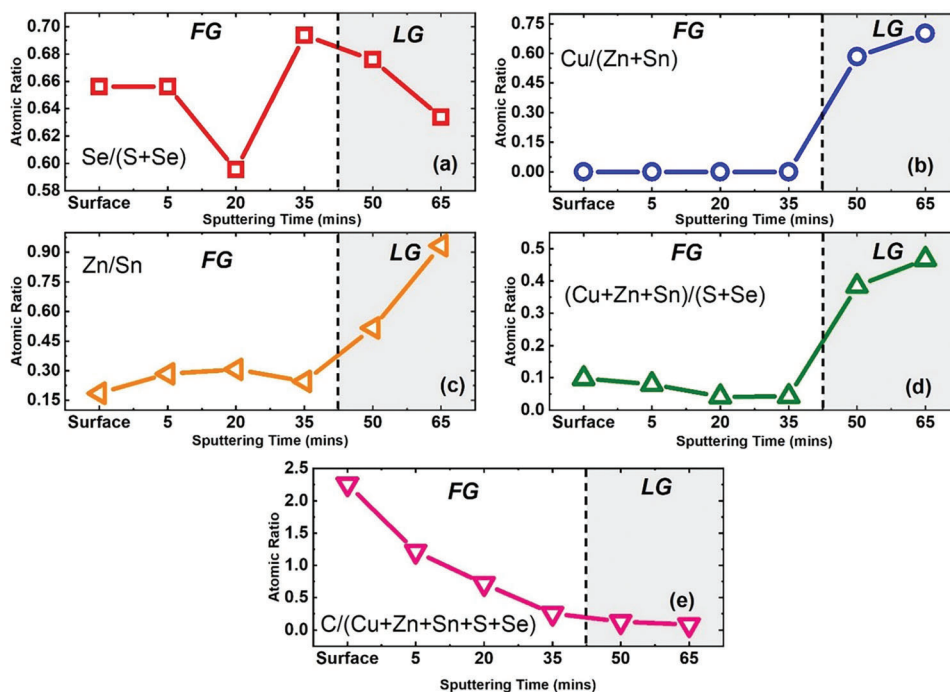


Figure 10. Elemental atomic ratio trend over sputtering time for a) $Se/(Se+S)$, b) $Cu/(Zn+Sn)$, c) Zn/Sn , d) $(Cu+Zn+Sn)/(S+Se)$, and e) $C/(Cu+Zn+Sn+S+Se)$.

3. Conclusion

A rapid, repeatable, and reliable PLO technique has enabled us to reveal the FG side of the CZTSSe layer developed by the hot injection nanoparticle synthesis method. A very high light intensity of 4 kW cm^{-2} pulsed for a short interval of 1 ms allowed the CZTSSe layer to be lifted-off from Mo coated substrate. The distinguishing features of the exposed FG side as compared to the LG region of CZTSSe film were mainly explored using XPS and ATR measurements. XPS depth profiling from the exposed rear surface of CZTSSe film was carried out through Ar^+ sputtering to develop an accurate understanding of the elemental composition variations and their effect on the formation of the FG sub-layer below the LG layer. A very high carbon content of around 70% was noticed at the rear surface of kesterite absorber while ATR result confirms the presence of sharp C—H bond signals due to the existence of bulky OLA-based ligands in the vicinity of nanocrystals, which is a cause of grain growth hindrance. Furthermore, the XPS depth profiling showed that there was no Cu signal up to 35 min of sputtering depth (labeled as FG) while Zn and Sn were also meagerly present in the FG layer, which depicted the importance of cations concentration for grains enlargement. Moreover, the total atomic content of C, S, and Se comprises more than 97% of the FG layer, which indicates the richness of secondary phases and charge blockage (due to low metallic content) near the back contact and is, therefore, expected to be detrimental for the solar cell performance. As part of future studies, the authors are focused on enhancing this research to find more insights about FG effects and experimentally further determine its implication on the device performance.

4. Experimental Section

Materials: Copper (II) acetylacetonate ($\text{Cu}(\text{acac})_2$, $\geq 99.99\%$), Zinc acetylacetonate ($\text{Zn}(\text{acac})_2$, $\geq 99.995\%$), tin (IV) bis(acetylacetonate) dichloride ($\text{Sn}(\text{acac})_2\text{Cl}_2$, $\geq 98\%$), elemental sulfur (S, $\geq 99.98\%$), oleylamine (OLA, technical grade) were all purchased from Sigma Aldrich and used as received. Toluene, Isopropanol (IPA), and 1-hexanethiol were analytical grades and purchased from Fisher Scientific.

Hot Injection Nanoparticle Synthesis: In the adopted solution-based method, CZTS nanoparticles were synthesized by injecting sulfur in a hot precursor solution. The precursor solution was prepared by adding $\text{Cu}(\text{acac})_2$ (1.34 mmol), $\text{Zn}(\text{acac})_2$ (0.95 mmol), $\text{Sn}(\text{acac})_2\text{Cl}_2$ (0.75 mmol) in OLA (10 mL). Such concentrations were used to achieve a Zn-rich and Cu-poor composition based on previous studies.^[13] This reaction was carried out in a three-neck flask connected to the Schlenk line. The temperature of the reaction was elevated to 225°C and sulfur (1 M) was injected through one of the inlets into the flask. Upon injecting sulfur, a decrease in solution temperature was noticed; hence, the temperature was elevated to 225°C again and the mixture was left to react for another 30 min, which would allow the growth of CZTS nanoparticles. As the reaction was completed, toluene (5 mL) and isopropanol (40 mL) were added to the solution. Thereafter, the solution was subjected to centrifuging and sonication process a few times in tandem. The collected CZTS nanoparticles were dispersed with the aid of sonication to provide CZTS nanoparticle inks with a concentration of $\approx 200 \text{ mg mL}^{-1}$ in 1-hexanethiol. The CZTS nanoparticle ink was then deposited on a soda lime glass substrate by slot die coating method. The parameters of the slot die coater were set to deposit multiple layers, yielding a $1 \text{ }\mu\text{m}$ CZTS film. Subsequently, this film was selenized in a tube furnace to convert CZTS nanoparticles into CZTSSe nanocrystals suitable for PV application. For this purpose, CZTS film was kept with selenium pellets (300 mg) in a graphite box enclosed

in a tube furnace chamber. The temperature of the chamber was kept at 500°C for 20 min to allow the reaction of selenium with CZTS film. After completion of the process, a greyish uniform CZTSSe surface was observed, which suggested a successful reaction of Se with the black-colored CZTS precursor film. Subsequently, 70 nm CdS was deposited using chemical bath deposition whereas 60 nm insulating-ZnO and 200 nm ITO were sputtered. Last, Ni—Al metal contacts are patterned by electronic beam deposition on the top. Further details of these layers are already provided in a previous work of the co-authors.^[13]

Absorber PLO: The PLO of the absorber layer from the Mo-coated glass substrate was carried out on a PulseForge Invent IX2-95X photonic curing system. This procedure involves the application of a high-energy pulse of light for a very short interval. The power of the laser is set such that most of the energy is absorbed at the back contact. The thermal expansion of Mo and MoSe_2 (having a higher thermal coefficient) at the back contact allows the CZTSSe layer to be released from the rigid substrate. Prior to the lift-off process, a 0.36 mm thick flexible and transparent polyurethane film was attached on top of the solar cell structure so that it would serve as a flexible substrate to the released layers post-lift-off process. The parameters of the photonic curer were set based on the COMSOL simulations which predicted a complete lift-off of the CZTSSe layer from the Mo substrate with a laser power density of 4 kW cm^{-2} pulsed for 1 ms.

Characterization Methods: XPS measurements were carried out by a Physical Electronics (PHI) 5000, Versaprobe instrument. The sample was excited with an Al K α monochromatic source with a gun power of 15 W to investigate elemental composition at the surface and inside the film. The instrument features a hemispherical analyzer where the pass energy was set to 58.7 eV and the spot size diameter was adjusted to 100 μm . The analyzer was positioned at an electron take-off angle of 45° . Depth profiling of the sample was done by a built-in Ar^+ sputtering gun for a total of 65 min with multiple intervals for measurement. Ar^+ ions were soft bombarded at 1 keV angled at 45° with respect to the sample surface, it is not expected that Ar^+ ions will alter the conclusions at such mild sputtering settings. For grazing incidence XRD measurements, a Siemens D-5000 diffractometer with a Cu K α radiation source ($\lambda = 0.154 \text{ nm}$) was used at a beam voltage of 40 kV and beam current of 50 mA in the parallel beam setup. In this work, a Tescan Mira 3 FEG SEM was used for SEM imaging together with an Oxford Instruments X-Max X-ray spectrometer fitted with a 20 mm^2 detector operating at 10–20 kV for EDS measurements. The IR spectrum was gathered by a Nicolet iS10 FTIR spectrometer (Thermo-Fisher Scientific). The instrument features a diamond crystal for ATR measurement. The IR signal was processed by Thermo Scientific OMNIC spectroscopy software. Raman spectroscopy was performed with a Horiba microscope using a 632.8 nm HeNe ion laser.

Supporting Information

Supporting Information is available from the Wiley Online Library or from the author.

Acknowledgements

A.J., M.J., and S.C. contributed equally to this work. This work was funded by the Scientific and Technological Council of Türkiye (TÜBİTAK), Grant No. 120N994 and British Council Newton Fund Institutional Links Grant (UK-Turkey) in Ultralight Absorber for Remote Energy Source, No. 623804307. The authors also acknowledge the Engineering and Physical Sciences Research Council (EPSRC) Centre for Doctoral Training in Renewable Energy Northeast Universities (ReNU) for funding through grant EP/S023836/1. The authors thank Dr. İlker Yildiz (Central Lab, METU) and Mr. Doğuşcan Dönmez for their assistance in XPS and ATR measurements, respectively.

Conflict of Interest

The authors declare no conflict of interest.

Data Availability Statement

The data that support the findings of this study are available from the corresponding author upon reasonable request.

Keywords

carbon-rich, depth profiling, fine-grain layer, kesterites, photonic lift-off, XPS

Received: August 28, 2023

Revised: October 3, 2023

Published online:

- [1] S. Hadke, M. Huang, C. Chen, Y. F. Tay, S. Chen, J. Tang, L. Wong, *Chem. Rev.* **2022**, 122, 10170.
- [2] D. B. Mitzi, O. Gunawan, T. K. Todorov, K. Wang, S. Guha, *Sol. Energy Mater. Sol. Cells* **2011**, 95, 1421.
- [3] H. Katagiri, K. Jimbo, W. S. Maw, K. Oishi, M. Yamazaki, H. Araki, A. Takeuchi, *Thin Solid Films* **2009**, 517, 2455.
- [4] M. Dianetti, F. Di Giacomo, G. Polino, C. Ciceroni, A. Liscio, A. D'epifanio, S. Licocchia, T. M. Brown, A. Di Carlo, F. Brunetti, *Sol. Energy Mater. Sol. Cells* **2015**, 140, 150.
- [5] T. T. Werner, G. M. Mudd, S. M. Jowitt, *Ore Geol. Rev.* **2017**, 86, 939.
- [6] L. Grandell, M. Hook, *Sustainability* **2015**, 7, 11818.
- [7] S. Wang, L. Huang, Z. Ye, L. Zhong, G. Chen, J. Li, X. Xiao, *J. Mater. Chem. A* **2021**, 9, 25522.
- [8] T. Taskesen, J. Neerken, J. Schoneberg, D. Pareek, V. Steininger, J. Parisi, L. Gütay, *Adv. Energy Mater.* **2018**, 8, 4.
- [9] S. Abermann, *Sol. Energy* **2013**, 94, 37.
- [10] A. Polman, M. Knight, E. C. Garnett, B. Ehrler, W. C. Sinke, *Science* **2016**, 352, aad4424.
- [11] X. Xu, Y. Qu, V. Barrioz, G. Zoppi, N. S. Beattie, *RSC Adv.* **2018**, 8, 3470.
- [12] T. Todorov, H. W. Hillhouse, S. Aazou, Z. Sekkat, O. Vigil-Galán, S. D. Deshmukh, R. Agrawal, S. Bourdais, M. Valdés, P. Arnou, D. B. Mitzi, P. J. Dale, *JPhys Energy* **2020**, 2, 012003.
- [13] Y. Qu, G. Zoppi, R. W. Miles, N. S. Beattie, *Mater. Res. Express* **2014**, 1, 045040.
- [14] Z. Gong, Q. Han, J. Li, L. Hou, A. Bukhtiar, S. Yang, B. Zou, *J. Alloys Compd.* **2016**, 663, 617.
- [15] Y. Qu, G. Zoppi, N. S. Beattie, *Prog. Photovoltaics Res. Appl.* **2016**, 24, 836.
- [16] P. R. Ghediya, T. K. Chaudhuri, *J. Mater. Sci.: Mater. Electron.* **2015**, 26, 1908.
- [17] V. A. Akhavan, B. W. Goodfellow, M. G. Panthani, C. Steinhagen, T. B. Harvey, C. J. Stolle, B. A. Korgel, *J. Solid State Chem.* **2012**, 189, 2.
- [18] H. Zhou, W.-C. Hsu, H.-S. Duan, B. Bob, W. Yang, T.-B. Song, C.-J. Hsu, Y. Yang, *Energy Environ. Sci.* **2013**, 6, 2822.
- [19] F. Liu, Q. Zeng, J. Li, X. Hao, A. Ho-Baillie, J. Tang, M. A. Green, *Mater. Today* **2020**, 41, 120.
- [20] W. Wang, M. T. Winkler, O. Gunawan, T. Gokmen, T. K. Todorov, Y. Zhu, D. B. Mitzi, *Adv. Energy Mater.* **2014**, 4, 1301465.
- [21] H. W. Hillhouse, M. C. Beard, *Curr. Opin. Colloid Interface Sci.* **2009**, 14, 245.
- [22] Q. Guo, H. W. Hillhouse, R. Agrawal, *J. Am. Chem. Soc.* **2009**, 131, 11672.
- [23] Y. Qu, G. Zoppi, N. S. Beattie, *Sol. Energy Mater. Sol. Cells* **2016**, 158, 130.
- [24] D. A. R. Barkhouse, O. Gunawan, T. Gokmen, T. K. Todorov, D. B. Mitzi, *Prog. Photovoltaics Res. Appl.* **2015**, 20, 6.
- [25] S. Suehiro, K. Horita, K. Kumamoto, M. Yuasa, T. Tanaka, K. Fujita, K. Shimano, T. Kida, *J. Phys. Chem. C* **2014**, 118, 804.
- [26] Y. E. Romanyuk, C. M. Fella, A. R. Uhl, M. Werner, A. N. Tiwari, T. Schnabel, E. Ahlswede, *Sol. Energy Mater. Sol. Cells* **2013**, 119, 181.
- [27] A. Carrete, A. Shavel, X. Fontané, J. Montserrat, J. Fan, M. Ibáñez, E. Saucedo, A. Pérez-Rodríguez, A. Cabot, *J. Am. Chem. Soc.* **2013**, 135, 15982.
- [28] Y. Qu, G. Zoppi, L. M. Peter, S. Jourdain, N. S. Beattie, *Jpn. J. Appl. Phys.* **2018**, 57, 08RC01.
- [29] X. Xu, Y. Qu, S. Campbell, M. Le Garrec, B. Ford, V. Barrioz, G. Zoppi, N. S. Beattie, *J. Mater. Sci. Mater. Electron.* **2019**, 30, 7883.
- [30] S. Campbell, M. Duchamp, N. Beattie, M. Jones, G. Zoppi, V. Barrioz, Y. Qu, in *2022 IEEE 49th Photovoltaics Specialists Conf.* (Eds.: B. Shafarman, K. Hinzer), IEEE, Philadelphia **2022**, p. 73.
- [31] D. Mutter, S. T. Dunham, *IEEE J. Photovoltaics* **2016**, 6, 562.
- [32] H. Ahmoum, M. Boughrara, M. S. Su'ait, G. Li, S. Chopra, Q. Wang, M. Kerouad, *Mater. Chem. Phys.* **2020**, 251, 123065.
- [33] K. Tanaka, M. Kato, H. Uchiki, *J. Alloys Compd.* **2014**, 616, 492.
- [34] S. Campbell, Y. Qu, L. Bowen, P. Chapon, V. Barrioz, N. S. Beattie, G. Zoppi, *Sol. Energy* **2018**, 175, 101.
- [35] W. Wu, Y. Cao, J. V. Caspar, Q. Guo, L. K. Johnson, I. Malajovich, H. D. Rosenfeld, K. R. Choudhury, *J. Mater. Chem. C* **2014**, 2, 3777.
- [36] M. Park, S. Ahn, J. H. Yun, J. Gwak, A. Cho, S. Ahn, K. Shin, D. Nam, H. Cheong, K. Yoon, *J. Alloys Compd.* **2012**, 513, 68.
- [37] J. Andrade-Arvizu, R. Fonoll-Rubio, Y. Sánchez, I. Becerril-Romero, C. Malerba, M. Valentini, L. Calvo-Barrio, V. Izquierdo-Roca, M. Placidi, O. Vigil-Galán, A. Pérez-Rodríguez, E. Saucedo, Z. Jehl Li-Kao, O. Vigil-gala, A. Pérez-Rodríguez, E. Saucedo, Z. J. Li-Kao, *ACS Appl. Energy Mater.* **2020**, 3, 10362.
- [38] E. Markauskas, P. Gečys, I. Repins, C. Beall, G. Račiukaitis, *Sol. Energy* **2017**, 150, 246.
- [39] P. D. Antunez, D. M. Bishop, Y. S. Lee, T. Gokmen, O. Gunawan, T. S. Gershon, T. K. Todorov, S. Singh, R. Haight, *Adv. Energy Mater.* **2017**, 7, 1602585.
- [40] P. D. Antunez, D. M. Bishop, Y. Luo, R. Haight, *Nat. Energy* **2017**, 2, 884.
- [41] B. Fleutot, D. Lincot, M. Jubault, Z. J. Li Kao, N. Naghavi, J.-F. Guillemoles, F. Donsanti, *Adv. Mater. Interfaces* **2014**, 1, 1400044.
- [42] D. Fuertes Marrón, A. Meeder, S. Sadewasser, R. Würz, C. A. Kaufmann, T. h. Glatzel, T. h. Schedel-Niedrig, M. C. h. Lux-Steiner, *J. Appl. Phys.* **2005**, 97, 094915.
- [43] E. Markauskas, P. Gecys, I. Repins, C. Beall, G. Raciukaitis, *Sol. Energy* **2017**, 150, 246.
- [44] S. J. Kim, H. E. Lee, H. Choi, Y. Kim, J. H. We, J. S. Shin, K. J. Lee, B. J. Cho, *ACS Nano* **2016**, 10, 10851.
- [45] B. Dang, P. Andry, C. Tsang, J. Maria, R. Polastre, R. Trzcinski, A. Prabhakar, J. Knickerbocker, in *Proc. – Electronic Components and Technology Conf.* (Eds.: J. Trwhella, D. McCann), IEEE, Las Vegas, **2010**, p. 1393.
- [46] G. J. Bauhuis, P. Mulder, E. J. Haverkamp, J. C. C. M. Huijben, J. J. Schermer, *Sol. Energy Mater. Sol. Cells* **2009**, 93, 1488.
- [47] C. H. Lee, D. R. Kim, I. S. Cho, N. William, Q. Wang, X. Zheng, *Sci. Rep.* **2012**, 2, 2.
- [48] M. M. A. J. Voncken, J. J. Schermer, G. J. Bauhuis, P. Mulder, P. K. Larsen, *Appl. Phys. A* **2004**, 79, 1801.
- [49] A. N. Tiwari, M. Krejci, F.-J. Haug, H. Zogg, *Prog. Photovoltaics Res. Appl.* **1999**, 7, 393.
- [50] A. M. Weidling, V. S. Turkani, V. Akhavan, K. A. Schroder, S. L. Swisher, *npj Flexible Electron.* **2022**, 6, 14.
- [51] W. Liu, V. S. Turkani, V. Akhavan, B. A. Korgel, *ACS Appl. Mater. Interfaces* **2021**, 13, 44549.
- [52] M. Mousel, A. Redinger, R. Djemour, M. Arasimowicz, N. Valle, P. Dale, S. Siebentritt, *Thin Solid Films* **2013**, 535, 83.

- [53] B. Canava, J. F. Guillemoles, J. Vigneron, D. Lincot, A. Etcheberry, *J. Phys. Chem. Solids* **2003**, *64*, 1791.
- [54] M. Bouttemy, P. Tran-Van, I. Gerard, T. Hildebrandt, A. Causier, J. L. Pelouard, G. Dagher, Z. Jehl, N. Naghavi, G. Voorwinden, B. Dimmler, M. Powalla, J. F. Guillemoles, D. Lincot, A. Etcheberry, *Thin Solid Films* **2011**, *519*, 7207.
- [55] K. J. Tiwari, R. Fonoll Rubio, S. Giraldo, L. Calvo-Barrio, V. Izquierdo-Roca, M. Placidi, Y. Sanchez, A. Pérez-Rodríguez, E. Saucedo, Z. Jehl Li-Kao, *Appl. Surf. Sci.* **2021**, *540*, 148342.
- [56] S. Campbell, M. Duchamp, B. Ford, M. Jones, L. L. Nguyen, M. C. Naylor, X. Xu, P. Maiello, G. Zoppi, V. Barrioz, N. S. Beattie, Y. Qu, *ACS Appl. Energy Mater.* **2022**, *5*, 5404.
- [57] Y. Qu, S. W. Chee, M. Duchamp, S. Campbell, G. Zoppi, V. Barrioz, Y. Giret, T. J. Penfold, A. Chaturvedi, U. Mirsaidov, N. S. Beattie, *ACS Appl. Energy Mater.* **2020**, *3*, 122.
- [58] D. Cozza, C. M. Ruiz, D. Duche, J. J. Simon, L. Escoubas, *IEEE J. Photovoltaics* **2016**, *6*, 1292.
- [59] S. Oueslati, G. Brammertz, M. Buffière, H. Elanzeery, D. Mangin, O. Eldaif, O. Touayar, C. Köble, M. Meuris, J. Poortmans, *J. Phys. D: Appl. Phys.* **2015**, *48*, 035103.
- [60] Selenium: XPS Periodic Table: Thermo Fisher Scientific – US, <https://www.thermofisher.com/tr/en/home/materials-science/learning-center/periodic-table/non-metal/selenium.html> (accessed: July 2023).
- [61] M. K. Bahl, R. L. Watson, K. J. Irgolic, *J. Chem. Phys.* **1980**, *72*, 4069.
- [62] H. Cai, L. Yao, Y. Xia, C. Dao, J. Li, L. Lin, Z. Huang, G. Chen, *Sol. Energy* **2019**, *193*, 986.
- [63] Y. Hamanaka, W. Oyaizu, M. Kawase, T. Kuzuya, *J. Nanoparticle Res.* **2017**, *19*, <https://doi.org/10.1007/s11051-016-3704-7>.
- [64] O. Stroyuk, A. Raevskaya, O. Selyshchev, V. Dzhagan, N. Gaponik, D. R. T. Zahn, A. Eychmüller, *Sci. Rep.* **2018**, *8*, 13677.
- [65] R. Mainz, B. C. Walker, S. S. Schmidt, O. Zander, A. Weber, H. Rodriguez-Alvarez, J. Just, M. Klaus, R. Agrawal, T. Unold, *Phys. Chem. Chem. Phys.* **2013**, *15*, 18281.
- [66] H.-Q. Xiao, W.-H. Zhou, D.-X. Kou, Z.-J. Zhou, Y.-N. Meng, Y.-F. Qi, S.-J. Yuan, Q.-W. Tian, S.-X. Wu, *Green Chem.* **2020**, *22*, 3597.
- [67] B. D. Chernomordik, A. E. Béland, D. D. Deng, L. F. Francis, E. S. Aydil, *Chem. Mater.* **2014**, *26*, 3191.
- [68] V. T. Tjong, Y. Zhang, J. Bell, H. Wang, *RSC Adv.* **2015**, *5*, 20178.